Baroclinic Turbulence in the Ocean: Analysis with Primitive Equation and Quasigeostrophic Simulations

ANTOINE VENAILLE AND GEOFFREY K. VALLIS

GFDL-AOS, Princeton, New Jersey

K. SHAFER SMITH

Center for Atmosphere Ocean Science, Courant Institute of Mathematical Sciences, New York University, New York, New York

(Manuscript received 14 December 2010, in final form 29 March 2011)

ABSTRACT

This paper examines the factors determining the distribution, length scale, magnitude, and structure of mesoscale oceanic eddies in an eddy-resolving primitive equation simulation of the Southern Ocean [Modeling Eddies in the Southern Ocean (MESO)]. In particular, the authors investigate the hypothesis that the primary source of mesoscale eddies is baroclinic instability acting locally on the mean state. Using local mean vertical profiles of shear and stratification from an eddying primitive equation simulation, the forced–dissipated quasigeostrophic equations are integrated in a doubly periodic domain at various locations. The scales, energy levels, and structure of the eddies found in the MESO simulation are compared to those predicted by linear stability analysis, as well as to the eddying structure of the quasigeostrophic simulations. This allows the authors to quantitatively estimate the role of local nonlinear effects and cascade phenomena in the generation of the eddy field.

There is a modest transfer of energy (an ''inverse cascade'') to larger scales in the horizontal, with the length scale of the resulting eddies typically comparable to or somewhat larger than the wavelength of the most unstable mode. The eddies are, however, manifestly nonlinear, and in many locations the turbulence is fairly well developed. Coherent structures also ubiquitously emerge during the nonlinear evolution of the eddy field. There is a near-universal tendency toward the production of grave vertical scales, with the barotropic and first baroclinic modes dominating almost everywhere, but there is a degree of surface intensification that is not captured by these modes. Although the results from the local quasigeostrophic model compare well with those of the primitive equation model in many locations, some profiles do not equilibrate in the quasigeostrophic model. In many cases, bottom friction plays an important quantitative role in determining the final scale and magnitude of eddies in the quasigeostrophic simulations.

1. Introduction

Altimetric observations of the sea surface (e.g., Fu and Menard 1983; Stammer 1997) reveal mesoscale eddies throughout the world's oceans, especially near western boundary currents and in the Antarctic Circumpolar Current (ACC). Mesoscale eddies are likely generated by baroclinic instability of the mean flow, gaining their energy from the massive potential energy reservoir associated with horizontal gradients of the mean stratification (Gill et al. 1974). The eddies dominate the oceanic kinetic energy (KE) and, through their effect on transport, play a major role in the general circulation. However, we do not have a well accepted consistent theory for their structure and statistics, especially in cases with realistic stratification, and eddies are not resolved in operational medium- and long-term climate forecasting models.

From the practical point of view, because they affect transport of heat, salt, and other tracers, unresolved eddies must be parameterized in climate forecasting models, and this need has yielded various parameterization schemes. A parameterization of mesoscale eddies attempts to mimic the turbulent flux that would arise had the eddies been resolved, and at the heart of any such scheme is a ''theory'' for the eddy statistics. However, even in the highly idealized case of two-layer quasigeostrophic (QG) flow driven

Corresponding author address: Antoine Venaille, GFDL, Forrestal Campus, Princeton, NJ 08540.
E-mail: venaille@princeton.edu

DOI: 10.1175/JPO-D-10-05021.1

by a horizontally homogeneous, time-independent mean flow, there is as yet no closed theory for the eddy statistics (for attempts and criticisms, see Held and Larichev 1996; Thompson and Young 2007). Time-dependent mean flows further complicate the picture (Farrell and Ioannou 1999; Flierl and Pedlosky 2007). To take into account the more complex local mean flows that arise in a general circulation model, parameterizations must therefore make rather drastic assumptions about the structure of the unresolved flow (e.g., Gent et al. 1995; Visbeck et al. 1997). However, even parameterizations that attempt to better account for the full vertical structure of the mean flow (e.g., Ferrari et al. 2010) still implicitly assume a horizontally local relationship between the resolved flow and the unresolved eddy fluxes; this will not be accurate if, for example, the eddying flow at a given location was generated elsewhere and advected in by the mean flow.

A great deal of work has been done both to understand how best to implement parameterizations in general circulation models and to understand the scale and magnitude of eddies generated by a given mean flow, but relatively little has been done to investigate the assumed local relationship. One approach, taken by Smith (2007b) and Tulloch et al. (2011), is to use the hydrographic or model mean state to compute local linear baroclinic instability scales and growth rates at each lateral, open-ocean location and to compare these directly to either observations or model output. If the dynamics is effectively close to that predicted by the local linear model, then these quantities would also characterize the observed eddy field. Not too surprisingly, only a rough, inconclusive correspondence between the observed field and the local linear prediction was found. Moreover, recent analyses of the altimetric data show that a large fraction of the mesoscale field is organized into coherent structures, such as rings (Chelton et al. 2007) and jet-like striations (Maximenko et al. 2005), which are likely the result of highly nonlinear processes.

Although it is more likely the case that the nonlinear evolution of the instability determines the eddy properties, the relationship between the mean state and the eddying flow may still be local. Of particular importance is the degree to which the nonlinear evolution of local baroclinic instabilities leads to an inverse cascade of energy, in both the horizontal and vertical. Altimetric observations do suggest that an inverse cascade to larger horizontal scales exists at the ocean surface (Scott and Wang 2005). However, determining which combination of vertical modes is sampled by the surface flow remains an open problem. Which modes are sampled by the observations is important for the following reasons: In the case of quasigeostrophic dynamics with two equal-depth layers, the classical picture of Rhines (1979) and Salmon (1980) is that baroclinic energy cascades toward the first baroclinic wavelength of deformation, at which point the baroclinic energy is transferred to the barotropic mode, and the barotropic energy then cascades toward larger scales, until finally dissipative mechanisms become effective. In this picture, the steady-state flow will be dominated by the barotropic mode. However, when realistic ocean stratification is present, the flow does not completely barotropize, except possibly on very long time scales, and a large portion of the energy remains in the baroclinic mode (Smith and Vallis 2001, 2002). This picture may be further modified by the presence of the ''surface quasigeostrophic'' mode (Lapeyre and Klein 2006), which undergoes its own inverse cascade (Capet et al. 2008).

As well as the vertical structure of the cascade and its projection on the observed surface, the structure of the evolved flow is also highly dependent on the nature of the mean potential vorticity (PV) gradient and the dissipation mechanism. Even relatively small gradients of the Coriolis parameter (the β effect) can result in a steady flow dominated by zonal jets (Rhines 1975; Vallis and Maltrud 1993). When the mean flow is not strictly zonal, as is the case in most oceanic locations, the eddy field may take on a very complex structure, still dominated by jets, but with extremely high eddy energy (Spall 2000; Arbic and Flierl 2004b; Smith 2007a). On the other hand, the presence of sufficiently strong drag may overwhelm the β effect and yield a nearly isotropic flow (Thompson and Young 2006, 2007). Finally, the nature of the drag term—quadratic versus linear—may also change the scale of the equilibrated flow (Arbic and Flierl 2004a; Grianik et al. 2004). In short, even when the flow is local and neglecting the effects of topography, variations in the local stratification, mean shear, and dissipation can result in a great diversity of possible equilibrated eddy fields.

In the present paper, we take a more direct approach and try to avoid the need for a complete theory of equilibrated mesoscale eddies in a homogeneous mean flow. Beginning with a high-resolution, eddy-rich ocean global circulation model simulation, we ask, to what extent is the steady-state eddy field at a particular location consistent with a homogeneous model of mesoscale turbulence? To address this question, we analyze the output from the $\frac{1}{6}^\circ$ run of the Modeling Eddies in the Southern Ocean (MESO) project (Hallberg and Gnanadesikan 2006), a series of simulations using an isopycnal primitive equation (PE) model. We consider first the statistical and structural properties of the eddy field throughout the model domain and perform a local stability analysis like that of Smith (2007b). We then choose a set of six locations and use the time-averaged mean fields at those locations to drive a horizontally periodic quasigeostrophic turbulence model to steady state. The primary metrics of comparison are (i) the horizontal length scale,

(ii) the magnitude, and (iii) the vertical structure of the eddy field: to what extent are these quantities consistent in the global circulation model and quasigeostrophic simulations?

The paper is organized as follows: section 2 is devoted to the studies of eddy properties in MESO simulations, with an emphasis on their vertical structure and a comparison with computations of linear baroclinic instability. Section 3 discusses the quasigeostrophic simulations carried out at various locations in the Southern Ocean. A comparison between eddies in MESO simulations and the forced–dissipated quasigeostrophic simulations is presented in section 4, and a summary is given in section 5.

2. Eddies in a comprehensive primitive equation ocean model

In this section, we examine the mesoscale turbulence in the eddy-resolving comprehensive primitive equation ocean model, specifically the 1/6° resolution MESO simulations of Hallberg and Gnanadesikan (2006). This is an isopycnal hemispheric ocean model with realistic geometry but somewhat idealized forcing.[1] There are 20 interior vertical layers and a three-level bulk mixed layer on the top.

a. Eddy properties in MESO simulations

The surface eddy kinetic energy (EKE_s) in MESO simulations, computed by considering a one-year time average of the square of velocity fluctuations, is presented in Fig. 1 (bottom). This map of EKE_s compares reasonably well with observations from altimetry (for more details, see Hallberg and Gnanadesikan 2006). It shows an inhomogeneous distribution of oceanic eddies: regions of high EKE are mostly located around western boundary currents and in some regions in the main body of the Antarctic Circumpolar Current (ACC).

A snapshot of the surface EKE in Fig. 1 (top) shows that these regions of high EKE_s correspond to regions where mesoscale turbulence tends to be organized into rings with typical velocities of 1 m s^{-1} and diameters L_{ring} of about 200 km. To extract coherent structures in an objective way from the eddy field, we employ the Okubo–Weiss parameter $W = 4[(\partial_x u)^2 + \partial_y u \partial_x v]$. This procedure has been used in previous diagnostics of altimetry measurements (Isern-Fontanet et al. 2003, 2006; Chelton et al. 2007). Coherent structures are found by looking for simply connected regions in which $W < -2 \times 10^{-12}$ s^{-2}, as in Chelton et al. (2007). The critical value must be sufficiently low to capture relevant coherent structures and sufficiently high to capture the whole area of a given coherent structure (Isern-Fontanet et al. 2006). We define the length scale L_{co} of a given structure as equal to the diameter of a disk that has the area of the coherent structure, $L_{\text{co}} = 2(\text{area}/\pi)^{1/2}$. In practice, this

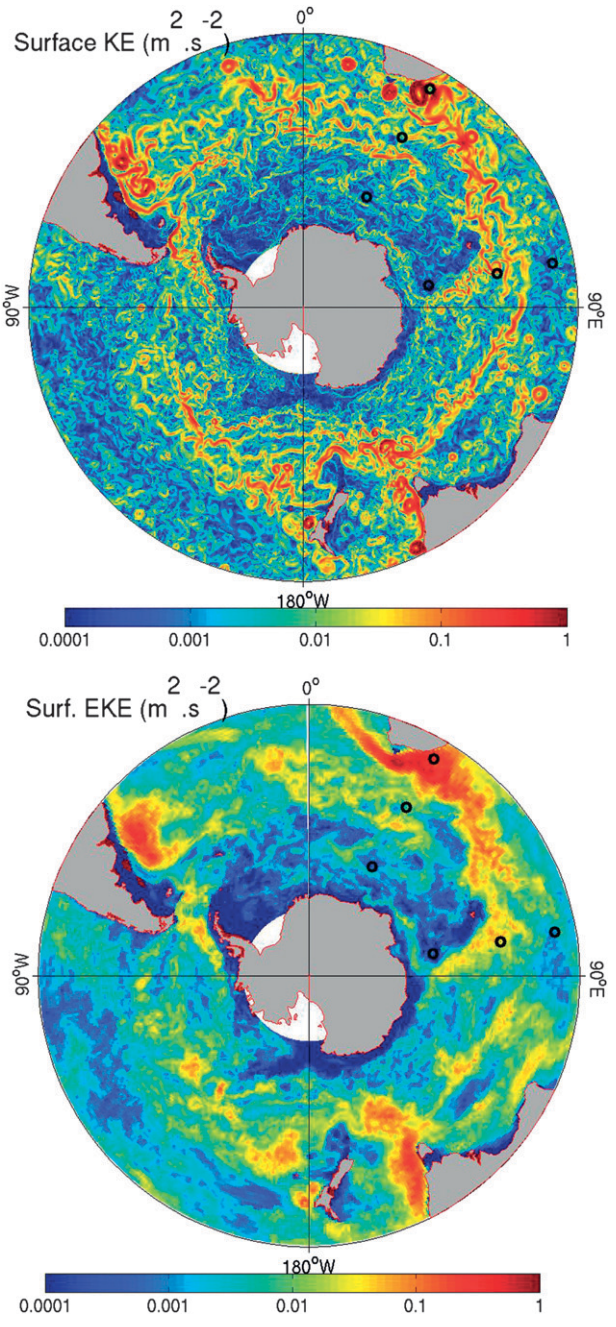

FIG. 1. (top) Snapshot of the surface KE (m^2 s^{-2}) plotted with a $\log_{10}$ scale. (bottom) One-year average of EKE_s from MESO simulations. The black circles correspond to the six locations considered for QG simulations; see Fig. 4 for the vertical structure of EKE at these particular points.

[1] For instance, there is no seasonal cycle in wind forcing.

criterion selects the core of the coherent structure and somewhat underestimates the length scale. The length L_{co} is therefore better considered as a convenient measure of the geographic variation of the eddy length scale rather than as an absolute measure of the eddy length scale itself. Both a snapshot and a one-year average of this quantity are plotted in Fig. 2. Similar to observations of eddies in the Mediterranean Sea by Isern-Fontanet et al. (2006), regions highly populated by large-scale coherent eddies are found in high EKE regions.

b. Modal projection of the eddy energy

To understand the broad characteristics of the vertical structure of the eddy field, we compute the vertical normal modes at each location. The baroclinic modes $\{\phi_m\}_{m\geq 1}$ are solutions of the Sturm–Liouville eigenvalue problem

$$\frac{d}{dz}\left(\frac{f_0^2}{N^2}\frac{d\phi_m}{dz}\right) = -\frac{\phi_m}{R_m^2}, \tag{1}$$

where $N(\text{lon}, \text{lat}, z)$ and $f_0(\text{lat})$ are the vertical profile of buoyancy frequency and the Coriolis parameter, respectively at a given location defined by its latitude and longitude. The boundary conditions for this problem are $d\phi_m/dz(z = 0) = d\phi_m/dz(z = -H) = 0$, where $H(\text{lon}, \text{lat})$ is the ocean depth at the location in question. To each baroclinic mode is associated an eigenvalue R_m^{-2} (lon, lat) defining the mth Rossby radius of deformation. For convenience, we also define the first deformation wavelength $L_1 \equiv 2\pi R_1$.[2] Note that the vertical modes provide a complete orthonormal basis for the vertical structure of any field satisfying the same boundary conditions. However, it has been recently argued that one should rather consider a basis that takes into account both the interior baroclinic modes and the surface-intensified modes that reflect the contribution from surface density gradients (Lapeyre 2009). Unfortunately, such a basis would not be orthonormal and would require more complicated analysis and interpretations, and therefore as a starting point we consider conventional baroclinic modes only; with a sufficiently high vertical resolution, these would also capture the surface-intensified modes, although the exploration of that is beyond the scope of the present paper.

Baroclinic modes and deformation scales are computed locally from the one-year-averaged density profiles. The problem (1) is discretized as in (Smith 2007b,

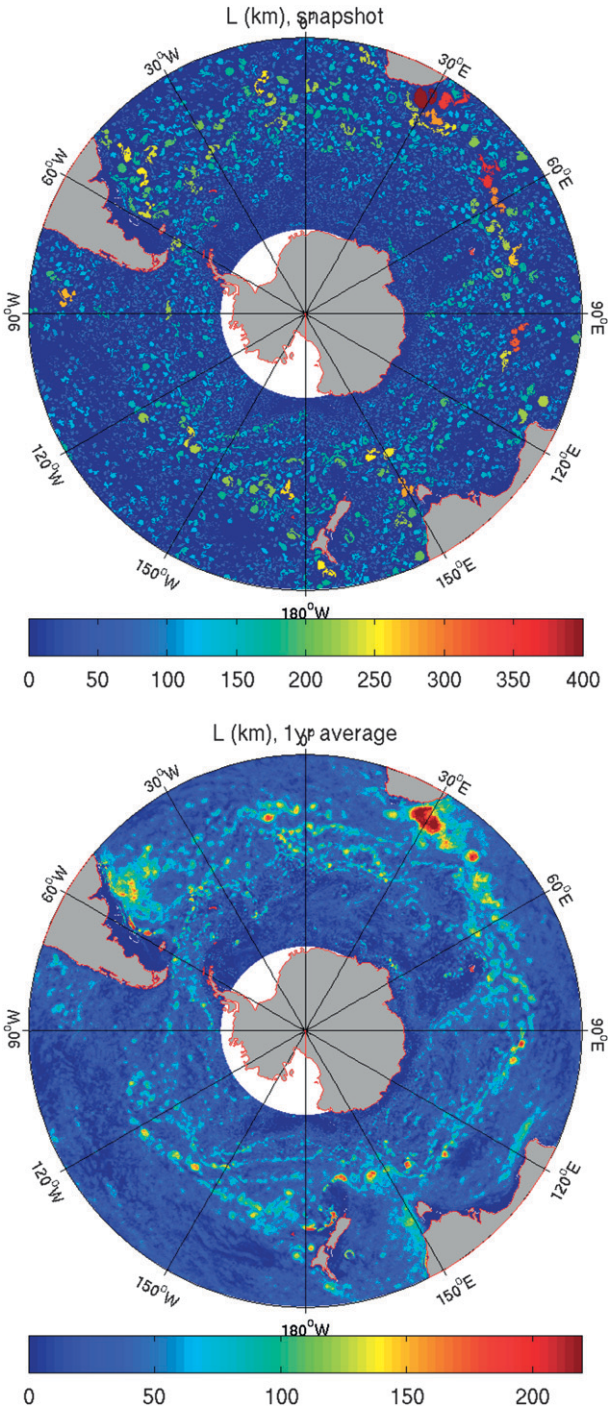

FIG. 2. (top) Core of the coherent rings extracted on a snapshot by using the Okubo–Weiss criterion; colors represent the equivalent diameter L_{co} of the coherent structures (see text for details). (bottom) One-year average of L_{co} represented as in (top). This allows us to define a global map of eddy length scale.

[2] Note that the above method of calculating the Rossby radius differs by a constant factor from the scaling estimate NH/f, even in the case of uniform stratification. In this case, it is readily shown that $R_1 = NH/(\pi f)$ and so $L_1 = 2NH/f$.

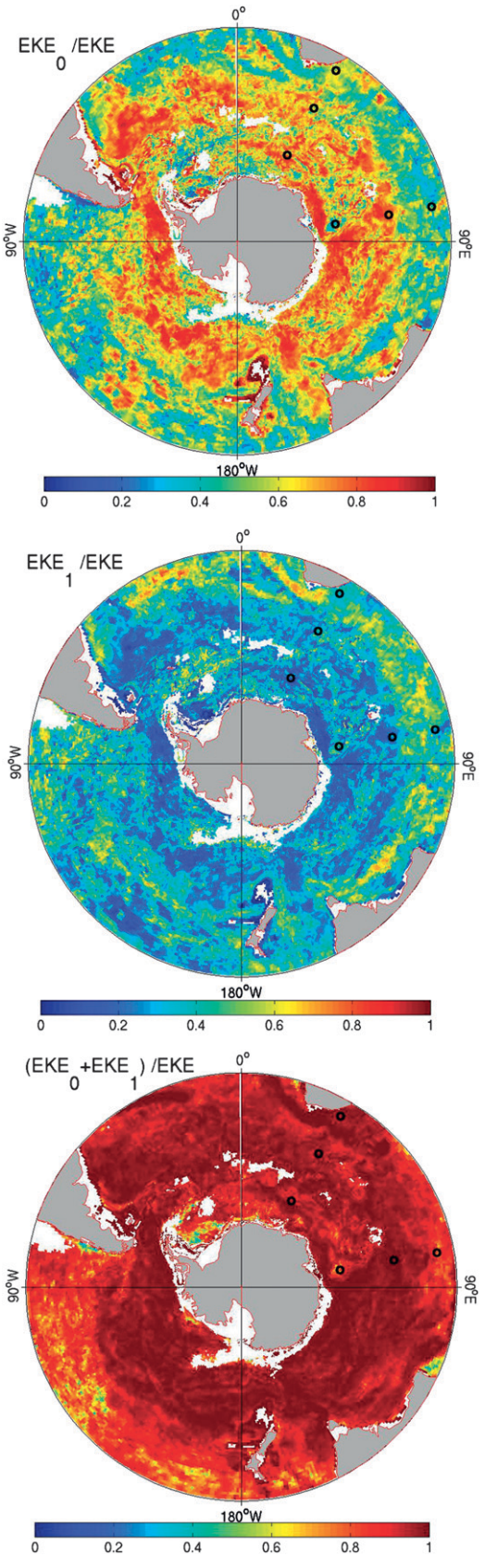

appendix A), and the particular discretization used here is the same as that in the MESO simulations, but with a minimum upper-layer depth of 30 m. Velocity fields are projected onto these modes at each point, and the partition of eddy kinetic energy into first baroclinic and barotropic modes is given in Fig. 3. Evidently, the EKE of the first baroclinic mode and of the barotropic mode accounts for nearly all the total EKE in MESO, typically well over 80%. The barotropic mode is clearly dominant along the ACC path, whereas the contribution of the first baroclinic mode becomes equivalent to the barotropic mode at lower latitudes. This is generally consistent with previous diagnostics by Wunsch (1997) on the vertical structure of eddies in the ocean, from (sparse) observations.

Vertical profiles of EKE at six different locations are plotted as in Fig. 4, and Table 1 gives additional information. Although EKE is in some places (e.g., at 34°S, 30°E, in the Aghulas Current) mostly barotropic and first baroclinic, the eddying field is in a number of places surface intensified in a way that cannot be explained by its barotropic and first baroclinic mode only (see the dashed blue lines of Fig. 4). That is to say, even though most of the energy does reside in the barotropic and first baroclinic modes, there is in some places a nonnegligible residual near the surface, possibly because of some form of surface instability or surface quasigeostrophic dynamics. A natural first question is then to determine if this vertical structure can be understood by linear instability computations of baroclinic instability around an imposed mean flow.

c. *Linear instability in the primitive equation simulations*

Following Smith (2007b), linear instability computations have been performed at each horizontal point of the MESO simulations (details are described in the appendix). The mean state is computed by taking a one-year time average over the entire flow. We chose the time period of one year after performing some preliminary analysis that showed that most unstable regions are characterized by fairly short instability time scales, from weeks to months. The mean flow is also varying on a similar time scale, and if we were to average over a much longer period the mean flow would be unrepresentative of the flow that the eddies actually see, whereas taking a smaller time average would leave a too-strong signature of the eddies in the mean fields. Taking a one-year average seemed the best choice,

←

FIG. 3. (top) Ratio of barotropic EKE to total EKE. (middle) Ratio of first baroclinic EKE to total EKE. (bottom) Sum of first baroclinic and barotropic contributions.

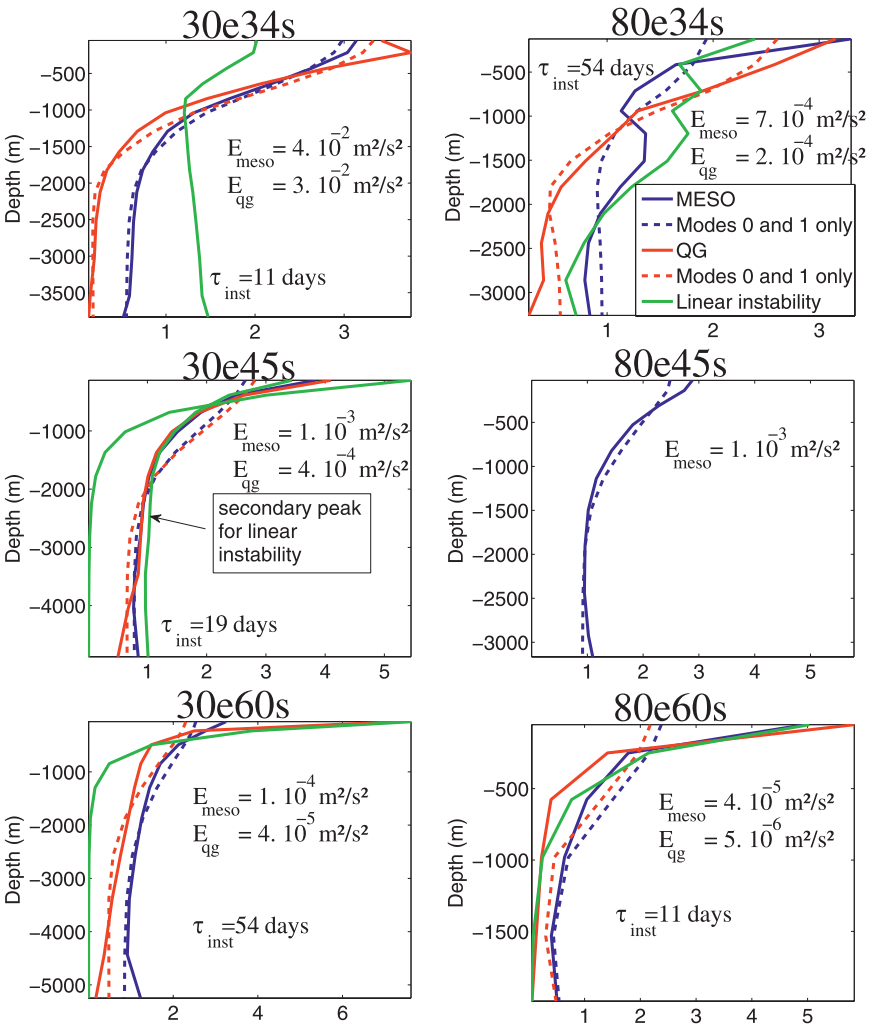

FIG. 4. Vertical EKE profiles in MESO (blue) and QG (red) simulations. Solid lines represent the EKE profile normalized by its average on the vertical; this allows us to compare the vertical structure on one side and the amplitude on the other. Values of the vertically averaged EKE are given in the different boxes for comparison. Dashed lines represent a reconstruction of the same EKE profile with the barotropic and the first baroclinic mode only, to determine how well the full profile is represented by considering only these two modes. The green solid line represents the squared norm of the amplitude of the most unstable linear mode, normalized by its vertical average. It would be the vertical EKE profile of the most unstable linear mode. At 45°S, 80°E, nonlinear QG simulations were found to be stable, so there is no QG simulation associated with this location.

and these fields are used in both the linear stability analysis and the nonlinear quasigeostrophic simulations described later.

The maximum instability growth rate $\omega_{inst} = 1/\tau_{inst}$ is plotted in Fig. 5 (top). Regions of fast growth in Fig. 5 are localized in space and are associated with large instability wavelengths $L_{inst} = 2\pi/(k_{inst}^2 + l_{inst}^2)^{1/2}$ (see appendix) in Fig. 6. These regions of fast growth mostly reflect the fine-grained structures of the mean flow and the localized regions of instability. This rough field is in some contrast with the rather smooth distribution of EKE in Fig. 1, which may reflect the smoothing out of localized instabilities by advective effects.

The ratio L_{inst}/L_1 is plotted in Fig. 5, and the first baroclinic Rossby radius R_1 is shown in Fig. 7. This ratio L_{inst}/L_1 is typically about 2 in the ACC and drops to about 0.3 at lower latitudes, except in regions of high growth rate, as for instance in western boundary currents. Note that, in the classical Eady problem (constant stratification and velocity shear and a flat bottom), $L_{inst}/L_1 \approx 2$ (Vallis

TABLE 1. This table summarizes properties of the most unstable mode at different locations, as well as nondimensional parameters, and some properties of EKE in MESO at these points. Here, $k^*_{\text{inst}} = 2\pi k_{\text{inst}}/L$ is the nondimensional instability wavenumber; with $L = 64R_1$, it gives $k^*_{\text{int}} \approx k_{\text{inst}}/(10R_1)\tau_{\text{inst}}$, which is the corresponding time scale (the inverse of the growth rate) in days. The terms A_0 and A_1 give the relative contribution of the amplitude of the unstable linear modes, as a percentage, to the barotropic and first baroclinic projections. Numbers in parentheses refer to secondary peaks in stability analysis. Throughput is $U_1/(r_bR_1)$, with $r_b = d_Ef/(2H)$, and criticality is $U_1/(\beta R_1^2)$. Here, E is the total EKE in MESO simulations at this point ($\text{m}^2\ \text{s}^{-2}$) and E_0^{MESO} and E_1^{MESO} give the relative contribution of the KE to barotropic and first baroclinic KE, respectively.

Location	k^*_{inst}	τ_{inst}	A_0, A_1	Throughput	Criticality	E^{MESO}	E_0^{MESO}, E_1^{MESO}
34°S, 30°E	6	11	97, 1	30	0.3	4×10^{-2}	61, 38
45°S, 30°E	16 (5)	16 (19)	16, 63 (79, 19)	20	5	1×10^{-3}	52, 41
30°S, 30°E	23 (4)	54 (90)	12, 42 (84, 4)	6	5	1×10^{-4}	71, 24
34°S, 80°E	19	54	87, 7	2	0.4	7×10^{-4}	49, 29
45°S, 80°E	5	60	88, 10	1	0.4	5×10^{-3}	72, 26
60°S, 80°E	14	11	32, 48	0.4	1.6	4×10^{-5}	32, 47

2006). The ACC is the region where the stratification is the closest to a linear profile, so it is not surprising that predictions based on the Eady problem are well approached. By contrast, small values of the ratio L_{inst}/L_1 are mostly associated with surface-intensified modes in regions where the mean flow is surface intensified and easterly sheared (Tulloch et al. 2011).

A major issue in the dynamics of mesoscale eddies in general and here in particular is understanding what sets their horizontal scale. Comparing the eddy properties in the fully developed primitive equation simulations with the linear stability properties (shown in Fig. 6), one finds that the simulated eddies tend to be a few times larger than the scale of the linear instability, but the interpretation is difficult because of the presence of structures in the field. The rings visible in Fig. 2 do seem to have diameters close to the instability wavelength in regions of fast growth: for example, Table 1 shows that the instability wavelength in the Aghulas Current (point 34°S, 30°E) is $L_{\text{inst}} \approx 2L_1 =$ 500 km, which is the about the size of oceanic rings in this region. Note that the way coherent structures are extracted tends to underestimate the eddy length scale, because our criterion on the Okubo–Weiss parameter selects the core of the rings. Note also that other metrics for the eddy length scale (for a discussion, see, e.g., Tulloch et al. 2011) would lead to similar conclusions.

The β effect is one possible and oft-cited mechanism that may play a part in setting eddy scales. In the presence of sufficiently large β, the flow will become anisotropic in the horizontal, possibly self-organizing into zonal jets (Rhines 1975; Vallis and Maltrud 1993) with widths on the order of the Rhines scale $(V/\beta)^{1/2}$, where V is some measure of the barotropic eddy velocity. Here, we define a Rhines wavelength as $L_{\text{Rh}} = 2\pi(v_{\text{rms}}/\beta)^{1/2}$, where v_{rms} is the root-mean-square meridional barotropic velocity; other choices do not change the results significantly. Figure 6 (bottom) shows the Rhines wavelength computed from the one-year average of the MESO simulation and shows that this scale is generally larger than both the instability wavelength and the ring size, taking on values of about 500 km in regions of high eddy activity. This is not surprising, because β becomes quite small at high latitudes, using an estimated value of $v_{\text{rms}} \sim 0.1\ \text{m s}^{-1}$ (appropriate to regions of high eddy activity, judging from Fig. 1) and β at 50° yields $L_{\text{Rh}} \sim$ 500 km. Moreover, the jets recently observed in the ocean (Maximenko et al. 2005; Richards et al. 2006) are typically at low latitudes: small jets in the ACC appear to be driven by topographic variations rather than β (Thompson 2010). Locally, oceanic eddy length scales tend to be closer to the scales given by linear instability analysis than the Rhines wavelength, but we should not conclude that the eddy field is a consequence of linear dynamics. The rings themselves are certainly nonlinear structures (for an interpretation of these structures as a result of potential vorticity homogenization with additional dynamical constraints, see, e.g., Venaille and Bouchet 2011), and their length scale is not necessarily given by local properties of the mean flow.

All these results are consistent with previous analysis of eddy length scale in terms of linear baroclinic instability (Tulloch et al. 2011). We note in addition that maps of eddy length scale, Rhines scale, and instability wavelength exhibit strong spatial inhomogeneities, with high values along western boundary currents. Caution is then warranted when interpreting zonal averages of such quantities.

As noted previously, the vertical structure of the eddies is primarily barotropic and first baroclinic, but there is in many places an additional intensification near the surface. Figure 4 shows, among other things, a comparison between the structure of vertical EKE profiles in the MESO simulation and the vertical profile of the energy of the fastest-growing linear mode $\text{EKE}_{\text{lin}}(z) = |\tilde{\psi}_{\text{inst}}|^2/\int_{-H}^{0} dz\ |\tilde{\psi}_{\text{inst}}|^2$, with arbitrary amplitude, at six particular locations. The surface intensification in both quantities suggests that at least part of this structure is a direct consequence of the linear instability

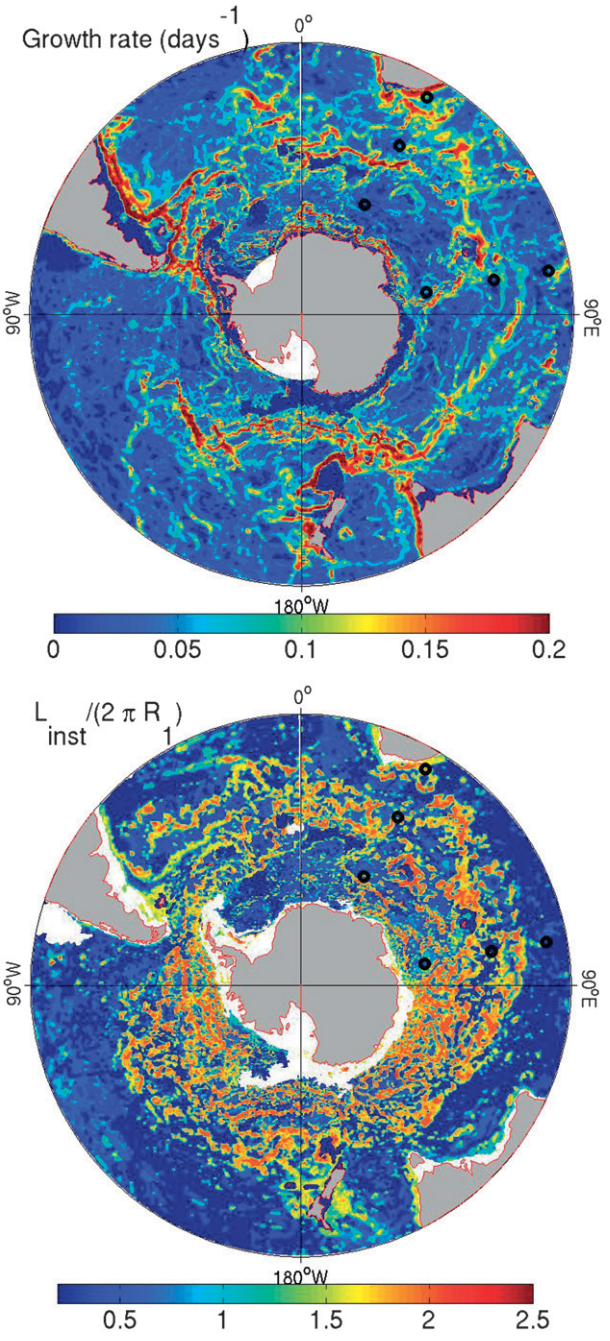

FIG. 5. (top) Growth rate of the most unstable mode, computed locally using one-year-averaged mean profiles from MESO simulations. Vertical structures of the corresponding amplitude are given for six points (represented by small black circles) in Fig. 4. (bottom) Ratio of the corresponding instability wavelength $L_{\text{inst}} = 2\pi/(k_{\text{inst}}^2 + l_{\text{inst}}^2)^{1/2}$ with the deformation wavelength $2\pi R_1$.

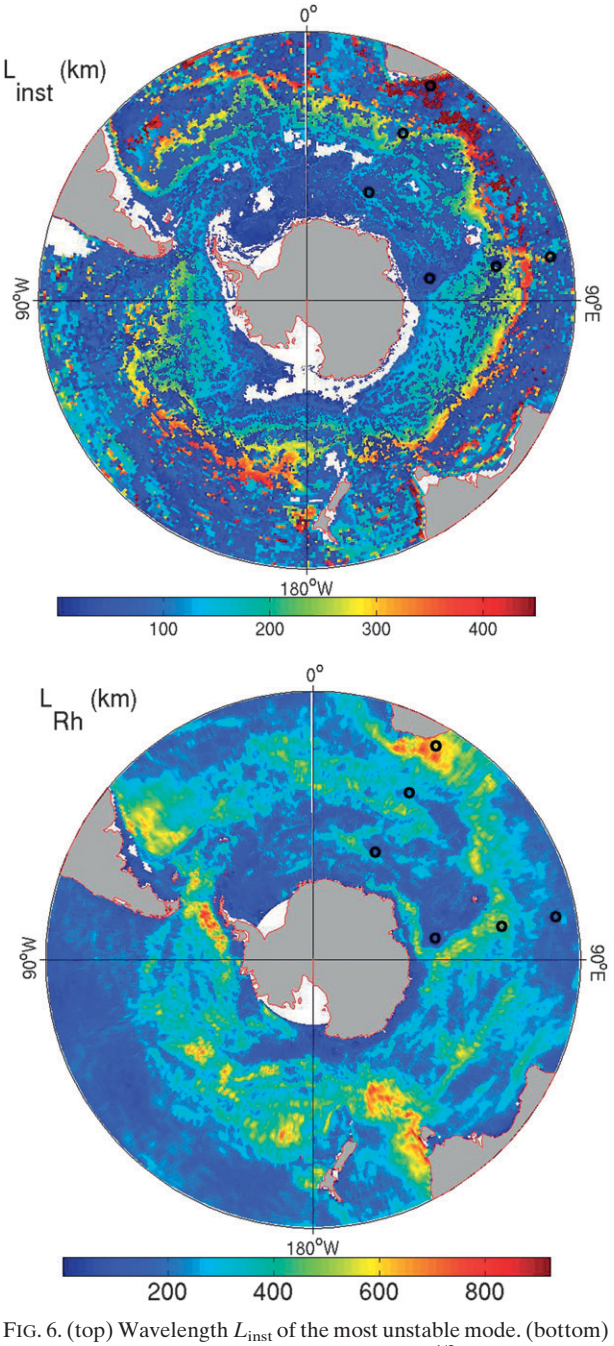

FIG. 6. (top) Wavelength L_{inst} of the most unstable mode. (bottom) Rhines scale $L_{\text{Rh}} = 2\pi(\upsilon_{\text{rms}}/\beta)^{1/2}$.

properties of the column. At the location 45°S, 80°E, there are eddies in the MESO field, despite the fact that linear analysis yields nearly stable modes (the growth rate $\sim 1/100$ days^{-1} and the scale of fastest growth $l_{\text{inst}} \sim L_1/50$ are both very small). Moreover, no eddy activity forms in the nonlinear quasigeostrophic model run with the mean flow at this location (discussed later), even after one year of integration. It seems likely that in this region eddies in MESO have their origin elsewhere and are advected in, rather than growing in situ.

Overall, the vertical structure of the EKE in the primitive equation simulations does have some resemblance to

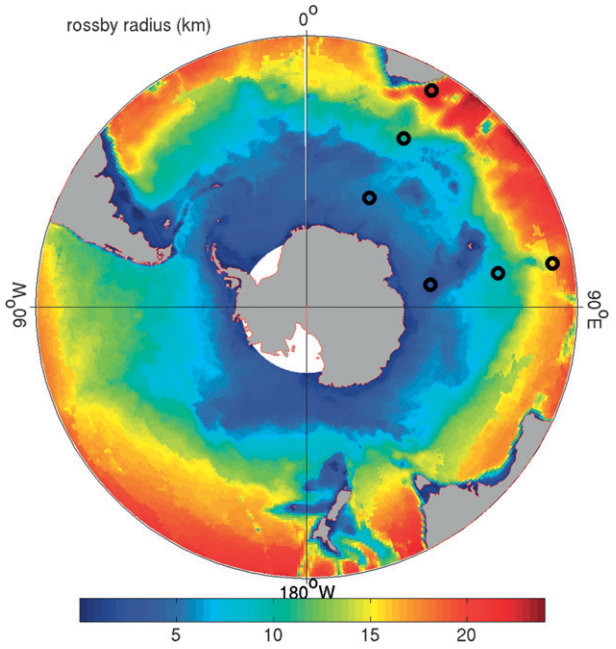

FIG. 7. Map of first baroclinic Rossby radius of deformation R_1.

linear dynamics, with surface intensification but otherwise a fairly uniform structure in the vertical. In the next section, we explore the extent to which the structure can be understood on the basis of quasigeostrophic turbulence.

3. Eddies in forced–dissipated quasigeostrophic simulations, with an imposed mean flow

We found that the eddy field in the primitive equation simulation bears some rough correspondence in vertical structure to that of the locally computed linear instabilities, but the horizontal eddy scales are larger and the spatial structures of the eddies are quite complex, including coherent vortices, jets, and turbulent undulations of streamlines. On the practical side, one would like a theory for the horizontal property flux the eddy field generates to effectively parameterize the effects of subgrid-scale eddies on a coarsely resolved ocean model. The eddy flux is a function of the eddy scale, energy, and vertical structure, and so a theory for the latter will yield the former.

However, there is no complete theory for the steady-state eddy statistics driven by an imposed mean state, even within the highly idealized assumptions of quasigeostrophic scaling and horizontal homogeneity (effectively equivalent to the use of a horizontally periodic domain). Attempts to form a theory for the steady-state, horizontally homogeneous eddy statistics in the case of two equal-depth layers and zonal-mean flow began with Haidvogel and Held (1980), and yet even these restrictions are insufficient to allow straightforward closure. Thompson and Young (2006) were able to construct a useful closure with $\beta = 0$ and a linear vorticity drag on the bottom layer, although their theory for the eddy diffusivity still required some empirical fitting. When nonzero β is included with zonal-mean flow, some progress was made by Held and Larichev (1996) and Lapeyre and Held (2003), although Thompson and Young (2007) suggest that the former results are problematic, in part because they do not explicitly take into account the role of drag in dissipating the energy, which has been known since at least Maltrud and Vallis (1991) to affect the inverse cascade. Furthermore, the possibility that the zonal flow is not uniformly eastward gives a rich phenomenology to the jets and eddies, as noted by Berloff et al. (2009b,a) for westward flows and Spall (2000) and Arbic and Flierl (2004b) for nonzonal-mean flows. Indeed, in some cases the flow cannot achieve a steady state (Smith 2007a). Nontrivial vertical structure and other drag mechanisms only add additional problems.

Our approach is therefore to use the steady-state statistics of a local model for the eddies as our theory, and this, in a nutshell, is the motivation for this section. Here, we consider nonlinear quasigeostrophic simulations of perturbations about imposed, baroclinically unstable mean states taken from six locations in the MESO run. The six locations are referenced in Tables 1 and 2 and represented as black circles in Fig. 1. We first review the quasigeostrophic model and describe its numerical implementation and then discuss the issues that arise in generating steady states with this model.

a. *Quasigeostrophic dynamics around imposed mean flows*

The perturbation quasigeostrophic PV is

$$q = \nabla^2\psi + \frac{\partial}{\partial z}\left(\frac{f_0^2}{N^2}\frac{\partial}{\partial z}\psi\right), \tag{2}$$

where ψ is the perturbation streamfunction and $\mathbf{u} = (-\partial_y\psi, \partial_x\psi)$ is the corresponding velocity perturbation. Neglecting contributions from the relative vorticity, the mean quasigeostrophic PV gradients are

$$\frac{\partial Q}{\partial x} = \frac{\partial}{\partial z}\left(\frac{f_0^2}{N^2}\frac{\partial V}{\partial z}\right), \quad \frac{\partial Q}{\partial y} = \beta - \frac{\partial}{\partial z}\left(\frac{f_0^2}{N^2}\frac{\partial U}{\partial z}\right), \tag{3}$$

where β is the planetary vorticity gradient and f_0 is the Coriolis parameter. The corresponding mean density profiles used in the six quasigeostrophic simulations presented here are plotted in Fig. 8, and the imposed mean velocity and PV gradient profiles are shown in Fig. 9.

TABLE 2. Summary of QG simulations. See text for details on the parameters of the "control" simulation. Here, r is bottom friction, υ_{th} is thermal drag (always zero unless specified), and E is the average KE ($m^2\ s^{-2}$). The terms E_0 and E_1 are the percentage of barotropic and first baroclinic energy. Here, k_{e0}, k_{e1}, and k_{ape1} give the peak of barotropic and baroclinic KE, as well as APE (in $2\pi/L$ unit, where $L = 64R_1$ is the domain size). The values of E^{MESO}, E_0^{MESO}, and E_1^{MESO} are given for comparison with output of MESO simulations.

Location	Feature	E	E_0, E_1	k_{e0}, k_{e1}, k_{ape1}	E^{MESO}	E_0^{MESO}, E_1^{MESO}
34°S, 30°E	Control	10*	86, 14	1, 5, 1	4×10^{-2}	61, 38
	$\beta = 0$	4*	92, 8	6, 6, 6	4×10^{-2}	61, 38
	$r = 100r_{control}$	2×10^{-1}	35, 63	4, 4, 4	4×10^{-2}	61, 38
	$r = 0.1r_{control}$	2×10^{2}*	99, 1	1, 1, 1	4×10^{-2}	61, 38
	$\upsilon_{th} = 10^{-4}$ days^{-1}	3×10^{-2}*	63, 34	4, 4, 4	4×10^{-2}	61, 38
34°S, 80°E	Control	2×10^{-4}*	32, 55	5, 5, 5	7×10^{-4}	49, 29
	$\beta = 0$	5×10^{-5}	42, 47	6, 6, 6	7×10^{-4}	49, 29
	$r = 100r_{control}$	6×10^{-4}*	48, 42	4, 4, 4	7×10^{-4}	49, 29
	$r = 0.1r_{control}$	6×10^{-4}*	70, 20	8, 4, 4	7×10^{-4}	49, 29
	$\upsilon_{th} = 10^{-5}$ days^{-1}	2×10^{-4}	32, 57	8, 8, 5	7×10^{-4}	49, 29
45°S, 30°E	Control	4×10^{-4}*	48, 43	6, 2, 2	1×10^{-3}	52, 41
	$\beta = 0$	1×10^{-2}	67, 29	2, 6, 4	1×10^{-3}	52, 41
	$r = 100r_{control}$	1×10^{-3}	43, 50	4, 4, 2	1×10^{-3}	52, 41
	$r = 0.1r_{control}$	9×10^{-2}*	97, 2	1, 6, 1	1×10^{-3}	52, 41
	$\upsilon_{th} = 10^{-4}$ days^{-1}	3×10^{-4}	46, 45	6, 3, 3	1×10^{-3}	52, 41
45°S, 80°E	Control	stable			5×10^{-3}	72, 26
	$\upsilon = 0$	3×10^{-5}	31, 59	4, 4, 3	5×10^{-3}	72, 26
60°S, 30°E	Control	2×10^{-5}*	29, 27	9, 9, 2	1×10^{-4}	71, 24
	$\beta = 0$	2×10^{-5}*	36, 41	4, 4, 4	1×10^{-4}	71, 24
	$r = 100r_{control}$	4×10^{-5}*	59, 29	5, 5, 4	1×10^{-4}	71, 24
	$r = 0.1r_{control}$	1×10^{-5}*	35, 28	8, 8, 5	1×10^{-4}	71, 24
	$\upsilon_{th} = 10^{-4}$ days^{-1}	4×10^{-5}*	46, 30	9, 9, 9	1×10^{-4}	71, 24
60°S, 80°E	Control	3×10^{-5}*	16, 42	2, 9, 2	4×10^{-5}	32, 47
	$\beta = 0$	2×10^{-6}	51, 43	4, 4, 2	4×10^{-5}	32, 47
	$r = 100r_{control}$	6×10^{-6}*	53, 38	2, 2, 2	4×10^{-5}	32, 47
	$r = 0.1r_{control}$	9×10^{-6}*	13, 36	13, 13, 9	4×10^{-5}	32, 47
	$\upsilon_{th} = 10^{-4}$ days^{-1}	5×10^{-6}	21, 40	5, 5, 5	4×10^{-5}	32, 47

* The simulation is not equilibrated.

The quasigeostrophic equation advection equation for the perturbation PVq given the imposed mean state $\mathbf{U}$, ∇Q is

$$\frac{\partial q}{\partial t} + (\mathbf{u} + \mathbf{U}) \cdot \nabla q + \mathbf{u} \cdot \nabla Q = 0 \qquad 0 > z > -H \quad \text{and} \tag{4a}$$

$$\frac{\partial}{\partial t}\frac{\partial \psi}{\partial z} + (\mathbf{u} + \mathbf{U}) \cdot \nabla \frac{\partial \psi}{\partial z} + \left(\mathbf{u} \times \frac{\partial \mathbf{U}}{\partial z}\right) \cdot \mathbf{k} = -N^2 w \qquad z = 0,\ -H, \tag{4b}$$

$$\text{with} \quad w(0) = 0 \quad \text{and} \quad w(-H) = -D_{bottom}, \tag{4c}$$

where D_{bottom} represents bottom friction (topography is omitted; see below) and $\mathbf{k}$ is the unit vector in the vertical direction. The boundary conditions (4b) can be formally replaced by the condition of no buoyancy variation at the top and the bottom layer ($\partial_z \psi = 0$ at $z = 0, -H$), provided that surface buoyancy anomalies are interpreted as a thin sheet of potential vorticity just above the ground and below the lid (Bretherton 1966). However, regardless of the formal representation of the boundary conditions, the accuracy of their numerical implementation depends strongly on vertical resolution. Note that the term $\mathbf{U} \cdot \nabla Q$ is omitted in Eq. (4a). This may be justified if there is scale separation between large-scale flow and perturbations (Pedlosky 1984) or if the mean flow is a steady state of the unforced undissipated quasigeostrophic equations. Although neither is strictly true in our case, following Arbic and Flierl (2004b) we do not expect quantitative changes to result from the presence of the term.

When dealing with nonlinear simulations of geostrophic turbulence, bottom topography may play an important role in that it may alter the vertical partitioning and variability of the eddy kinetic energy by coupling vertical modes together (e.g., Treguier and Hua 1988; Treguier and McWilliams 1990). In addition, closed contours of bottom topography may lead to the formation of coherent vortices (e.g., Dewar 1998; Merryfield 1998), and the presence of topographic beta effect may affect jet spacing and distribution (e.g., Sinha and Richards 1999). In this study, we omit bottom topography primarily as a simplification, but we recognize its

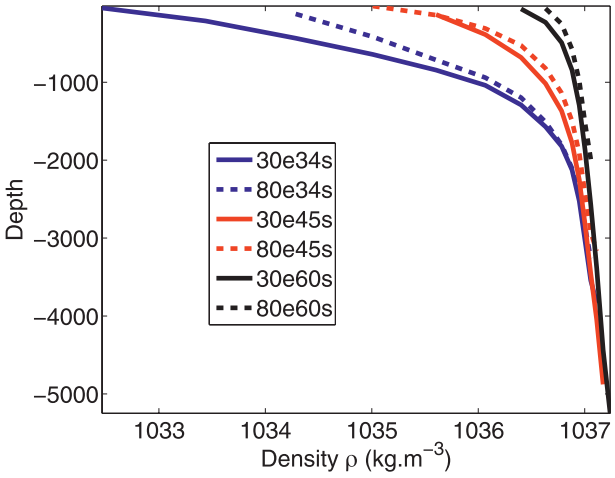

FIG. 8. Density profiles from one-year-averaged MESO simulations, at the six locations considered for the QG simulations.

potential importance. We do note that the presence of nonzonal-mean flows extracted from a temporal average of the primitive equation ocean model is mostly due to topographic steering (e.g., Marshall 1995). In that sense, one may argue that topography is implicitly present in the forcing term of our quasigeostrophic simulations.

The quasigeostrophic simulations were performed in a doubly periodic domain of extension $L = 64R_1$ (where R_1 is the first deformation radius), using a spectral code in the horizontal and finite-difference in the vertical (for details, see Smith and Vallis 2002). All the runs presented in this paper have an effective resolution of 256^2 in the horizontal and vertical resolution that varies from place to place, depending on the average number of layers present at that location in the MESO simulation (typically from 7 to 16). Integrations were performed until a statistically steady state was achieved. The equilibration times were found to be extremely large, requiring typically more than 15 yr. This difficult equilibration was already reported in the same framework, but for even more idealized settings, by Arbic and Flierl (2004b). When equilibration was not possible over this period of time, additional dissipation mechanisms were included (see the next section for more discussion of this choice).

b. *Effect of the mean state parameters and structure on the steady-state perturbation flow*

Steady state is achieved when eddy energy generation by the unstable mean flow is balanced by dissipation. Multiplication of (4a) by $-\psi$ and integration over the periodic domain yields the eddy energy budget

$$\frac{dE}{dt} = \int dz\, V\overline{uq} - U\overline{vq} - \text{dissipation}. \qquad (5)$$

Generation of eddy energy thus occurs through the eddy flux of PV, and the dissipation term depends on the bottom drag D_{bottom}. Because eddy energy tends to accumulate in low-mode, large-scale flows, the most energy effective dissipation mechanisms are either scale independent or concentrated at large scales; in the present simulations, we primarily use linear (scale independent) bottom drag. The numerical simulations also include a small-scale enstrophy dissipation filter, but this has negligible effects on the energy budget.

1) THE BETA EFFECT

The Coriolis gradient β yields a constant term in the meridional mean PV gradient, $\partial_y Q = \beta - \partial_z[(f_0/N)^2\partial_z U]$. Profiles of mean PV gradients at six different locations are given in Fig. 9. Typically, variations of the mean PV gradient due to thickness (or stretching) variations are much stronger than β in the locations considered (as in Smith 2007b), and linear instability computations depend only a little on β at these points. The effect of β would have been much more important if we had considered the linear instability due to just the barotropic and first baroclinic modes (i.e., if we had projected the mean shear onto just the first two modes), the equivalent of a two-layer model. For instance, defining the two-layer criticality number as $\text{Cr} = U_1/\beta R_1^2$, where U_1 is the projection of the mean zonal velocity on the first baroclinic mode, gives values on the order of one (see Table 1), but this definition does not take into account the strong vertical variations of mean PV gradients, which overwhelm β.

The relative unimportance of β from the point of view of linear stability contrasts with the strong qualitative differences between simulations performed with and without β at almost every location (see Table 2). The energy levels in the nonlinear simulations are sometimes greater with β than without it, which from a linear perspective is perhaps somewhat surprising. A similar result was found for nonzero mean meridional flows by Spall (2000), and the result stands in contrast to the effect of β on cases with purely zonal flow. In the zonal-mean flow case (with predominantly zonal flow directed eastward in upper layers relatively to the lower layers), increasing β has a stabilizing effect for linear modes, and consistently the scaling of Held and Larichev (1996) predicts a decrease of energy production with β in forced–dissipated simulations.

The reasons for the contrasting roles of β in zonal- and nonzonal-mean flow can actually be well understood through its tendency to produce zonally elongated flows (rather than its effect on stability), which then affects the eddy generation terms in (5) in different ways. When β is large enough to produce eddy-driven zonal jets (e.g.,

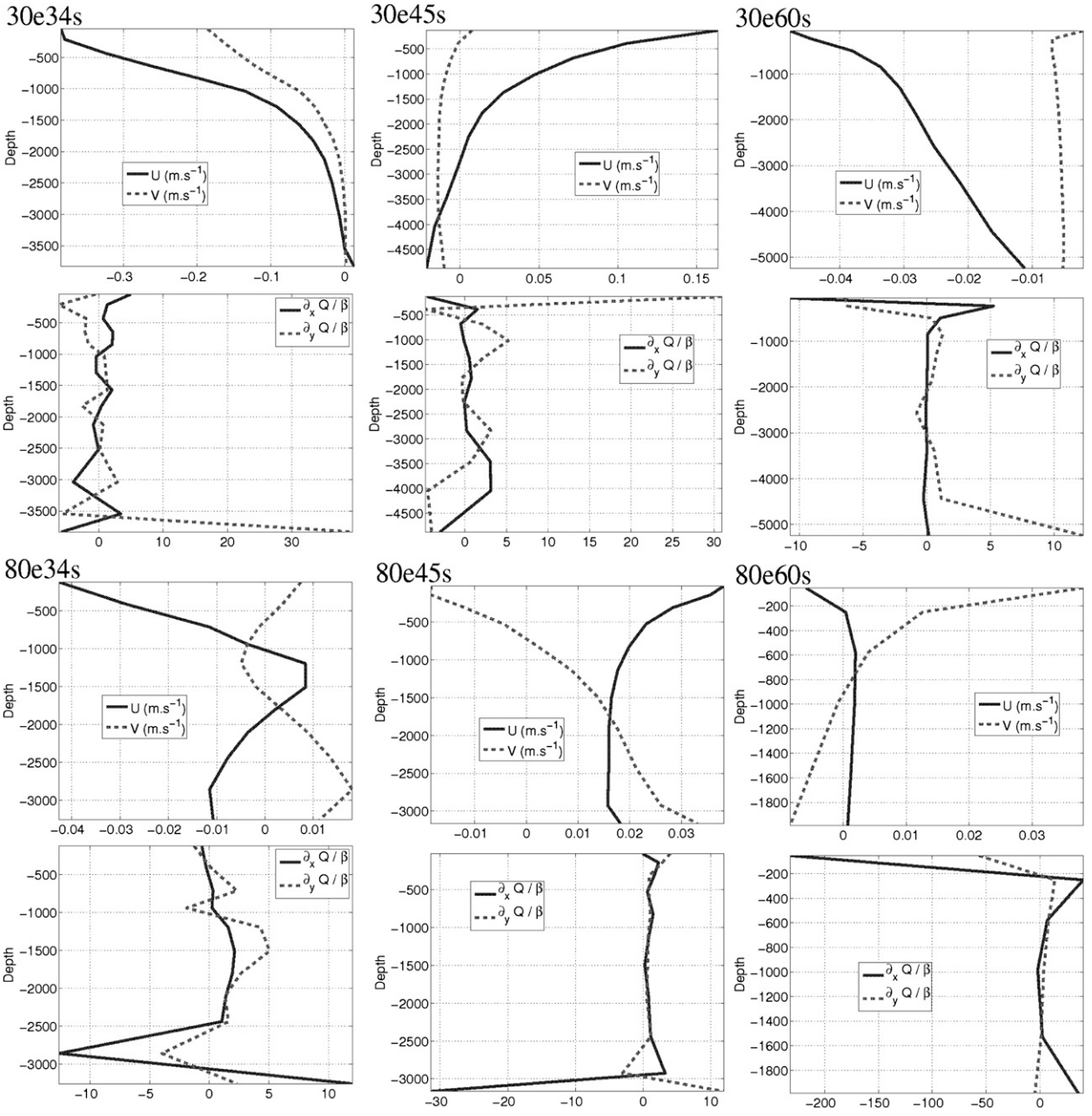

FIG. 9. Mean vertical profiles of (top panels in each set) velocity and (bottom panels in each set) PV gradients at the six different locations used for the QG simulations. Velocities are in m s^{-1}, and PV gradients are in units of β. Note that the horizontal and vertical axes are not the same for the different locations.

when drag is small enough to allow zonal anisotropies to form), the northward (cross jet) PV flux $\overline{vq}$ is suppressed, because cross-jet fluxes tend to be increasingly suppressed as the jet strengthens (Smith 2005; Haynes et al. 2007). By contrast, as the jets increase in strength, correlations arise between potential vorticity q and zonal velocities u, resulting in an enhanced eastward (along jet) PV flux $\overline{uq}$. When both U and V are nonzero, increasing β will lead to stronger jets, and eddy energy injection due to the along-jet flux ($\int dz\, V\overline{uq}$) will far dominate the increasingly negligible across-jet flux due to the zonal flow ($-\int dz\, U\overline{vq}$); thus, when the flow is more nonzonal, eddy energy will increase with β (Smith 2007a). In some of the locations investigated here, this enhanced production of eddy energy due to nonzonal-mean flow prevented equilibration in the quasigeostrophic simulation.

2) THE ROLE OF BOTTOM FRICTION

In addition to the complexities encountered with the combination of β and nonzonal-mean flows, reliance on bottom drag can also make equilibration difficult to achieve. In cases in which the dynamics is confined to the upper ocean and with no efficient energy transfers from these upper layers to the lower layers, bottom friction may not be sufficient to achieve equilibration (Arbic and Flierl 2004b). In the real ocean, energy may also dissipate either by eddies propagating away from the region of generation and by small-scale dissipation by nongeostrophic processes in the ocean interior. In some cases, we sought to achieve equilibration by the addition of another dissipative process: namely, a small thermal drag of the form $\nu_{\rm th}\partial_z((f_0/N)^2\partial_z\psi)$ on the right-hand side of the PV transport Eq. (4a). This term damps vertical variations of buoyancy, allowing for the equilibration of simulations that are significantly influenced by the growth of available potential energy (APE). This is the case, for example, when eddies are organized into surface-intensified zonal jets separating regions of quasi-homogenized potential vorticity: the total energy is dominated by the APE of the homogenized regions, whereas the kinetic energy, dominated by the jets at the interfaces, was quasi equilibrated.

A nondimensional parameter one can associate with bottom friction is the throughput $U_1/R_1 r_b$, where r_b is the bottom friction coefficient. In the limit of small bottom velocities, the bottom drag is an approximation to the Ekman drag, and $r_b \sim d_E f/2H$, where d_E is the Ekman layer depth. Control experiments assumed a typical Ekman layer depth on the order of 10 m, which leads to throughput values from 0.5 to 30 in the six locations considered (see Table 1). The fact that some simulations were difficult to equilibrate and many uncertainties were attached to the estimation of the depth of bottom Ekman layer motivated us to carry out a number of other simulations in which the Ekman layer depth is fixed at 1, 100 (not shown in this paper), and 1000 m. These values (some of them being unrealistic for the ocean) span the limits of very weak and very strong bottom friction. Note that the bottom drag force is parameterized as $\mathbf{F}_{\rm bot} = C_d(u_{\rm bot}^2+u_c^2)^{1/2}\mathbf{u}_{\rm bot}$ in the MESO simulations (Hallberg and Gnanadesikan 2006). However, the friction term in MESO simulations involves the total velocity (eddies plus mean flow) so that a quadratic friction for the quasigeostrophic simulations would in general not be equivalent to the quadratic friction of the primitive equation simulations. In fact, use of a linear drag is more or less equivalent to the bottom drag used in MESO simulations whenever the bottom velocity is smaller than approximately 0.05 m s^{-1}.

As expected from previous numerical computations of geostrophic turbulence in two-layer models, bottom friction plays an important role in setting the horizontal and vertical structure of the turbulence (Arbic and Flierl 2004a; Thompson and Young 2007). This is illustrated in Table 2 by the changes in the contribution of barotropic and first baroclinic modes with different values of bottom friction. The ratio of the baroclinic to barotropic kinetic energy tends to zero in the limit of vanishing bottom friction, whereas it tends to a constant value in the limit of high bottom friction, consistent with previous forced–dissipated simulations of two-layer quasigeostrophic models (Arbic and Flierl 2004a).

The complete barotropization in the low-friction limit can be understood as a tendency for the system to reach the gravest modes, consistently with the Rhines–Salmon phenomenology of two-layer turbulent flow. In the high-friction limit, bottom drag strongly damps the dynamics in the lower layers. If one combines the condition of vanishing velocity at the bottom and the tendency for the system to reach the gravest vertical mode, then the energy will project mostly on the barotropic and the first baroclinic mode in such a way that the baroclinic mode compensates the barotropic mode at the bottom. The ratios of barotropic to baroclinic energy in MESO (see Table 1) and in the quasigeostrophic simulations (see Table 2) show that the ocean is in an intermediate regime between these two limits.

4. Comparison between primitive equation and quasigeostrophic simulations

a. Eddy kinetic energy levels and vertical structure

A comparison of eddy kinetic energy levels in the MESO simulation (see Table 1) and the equilibrated quasigeostrophic simulations (see Table 2) shows some of the strengths and limits of the locality hypothesis. Some regions of high energy levels in MESO are also regions of high energy levels in quasigeostrophic simulations, but in other regions (see, e.g., point 34°S, 30°E in the Aghulas Current) energy levels produced in the quasigeostrophic simulations are orders of magnitude higher than MESO simulation (or it was necessary to consider artificially high bottom drag to obtain similar values). On the other hand, regions of low energy levels in MESO are always found to be regions of low energy levels in quasigeostrophic simulations; in fact, the energy levels produced in quasigeostrophic simulations are smaller than in MESO simulations. These results suggest that a few very energetic regions supply eddies to other, less baroclinically active regions, although the existence of missing energy sources (such as mixed baroclinic–barotropic instabilities or direct generation by winds) and sinks (such as ageostrophic processes) in

the QG models forced by baroclinic instability make such an assertion a little tentative.

The normalized profiles of EKE extracted from the QG simulations at the six different locations are presented in Fig. 4. Also shown are the corresponding EKE profiles from the same locations in the MESO simulation, as well as EKE profiles because of only to the barotropic and first baroclinic mode (see also Table 2). In some places, there is a clear tendency for energy to accumulate in low modes (at points 34°S, 30°E and 34°S, 80°E), whereas in others the vertical structure is similar to that of the most unstable mode, sometimes enhanced near the surface.

b. Eddy length scale and horizontal structure

To compare the horizontal organization of mesoscale turbulence between the two models, snapshots of surface flows are presented in Figs. 10 and 11. Snapshots of the MESO simulation (in which the time-mean flow is removed) are chosen such that the point at which the vertical profiles are extracted for the quasigeostrophic simulation is at the center of the domain. The domain length scale is the same as for the quasigeostrophic simulations: namely, $L = 64R_1$, where R_1 is the first baroclinic Rossby radius of deformation at this point. In each case, MESO snapshots are compared with the quasigeostrophic simulations that are equilibrated (see Table 2), even if the equilibration involves high bottom friction or the use of thermal damping. Because point 45°S, 80°E was found to be stable and because none of the 60°S, 30°E simulations were equilibrated, the dynamics at these locations are not discussed in the following. Perhaps the most noticeable feature is the emergence of structures of one form or another in nearly all cases.

Point 34°S, 30°E is located in the western boundary current along South Africa, perhaps the most energetic region of the ocean. A typical feature of eddying activity in this region is the formation of mesoscale rings, which is visible in Fig. 10 (left). Strikingly, the (all anticyclonic) rings produced in the quasigeostrophic simulations are of similar size, slightly larger than the wavelength of the most baroclinically unstable mode. This quasigeostrophic illustration is taken from a run with high bottom friction ($r = 100r_b$ in Table 2). Decreasing the friction to $r = 10r_b$ leads to an increase of the number of rings, and their length scale is then equal to the instability wavelength. In this case, the flow looks very similar to the ''vortex crystal'' observed previously in the two-layer quasigeostrophic simulations of Arbic and Flierl (2004b) and in simulations of the Euler equations with both random and deterministic forcing (Jiménez and Guegan 2007). In our simulations, when either the (westward) zonal-mean shear or the meridional mean shear were set to zero, no vortex crystals were observed. For lower bottom friction (r_b and $0.1r_b$ on Table 2), there remains only one vortex at the scale of the instability wavelength, whereas the flow is dominated by a single domain scale barotropic vortex. This implies that the scale of the eddies is a nonmonotonic function of bottom friction, consistent with the results of Thompson and Young (2006). Note that both the westward component of the mean shear and a nonzero meridional velocity were needed to produce these rings.

Barotropic instability and topographic interactions are not present in the quasigeostrophic simulations; evidently, baroclinic instability and nonlinear evolution are sufficient to create the coherent rings, with comparable length scales to the observed rings in MESO simulations. That is, their formation is the result of self-organization and they are not shed from zonal jets. In the particular case of location 34°S, 30°E, the mean flow is close to the western boundary current and the formation of the rings in the primitive equation simulation is almost certainly affected by the coastline. However, although less pronounced, the formation of such rings occurs in both the QG and PE simulations performed in other regions, far from boundary currents. This spontaneous self-organization of the flow into rings can be observed in movies of MESO simulations, which are available from the authors.

At 45°S, 30°E (Fig. 11, left), both the MESO and the QG simulation show rings embedded between coherent, relatively strong eastward jets. It seems likely that the jet structures observed in MESO (and in the real ACC) are due to the effects of topography, whereas the jets found in the QG simulation are likely consequences of the low energy state of the run. Other energy dissipation mechanisms or nonlocal effects might allow a higher equilibrated energy level that suppresses β-driven jets. In addition, the rings are larger in MESO than in the QG simulation. This may be a consequence of the fact that the total kinetic energy of the QG run is about one-third that of the same region in the MESO simulation, resulting in smaller structures in the QG simulations. Another possibility is that larger rings might come from other regions in MESO simulations.

c. Is there an inverse cascade?

Do the energy-containing eddies have a scale larger than the instability wavelength? Here, we regard the latter as corresponding to the injection wavelength in forced–dissipated quasigeostrophic simulations. There are then two different but related scales we consider: the scale of the KE and the scale of the APE. Equivalently, we may also consider the energy in the barotropic mode (entirely kinetic) and the energy in the first and higher baroclinic modes (kinetic plus potential).

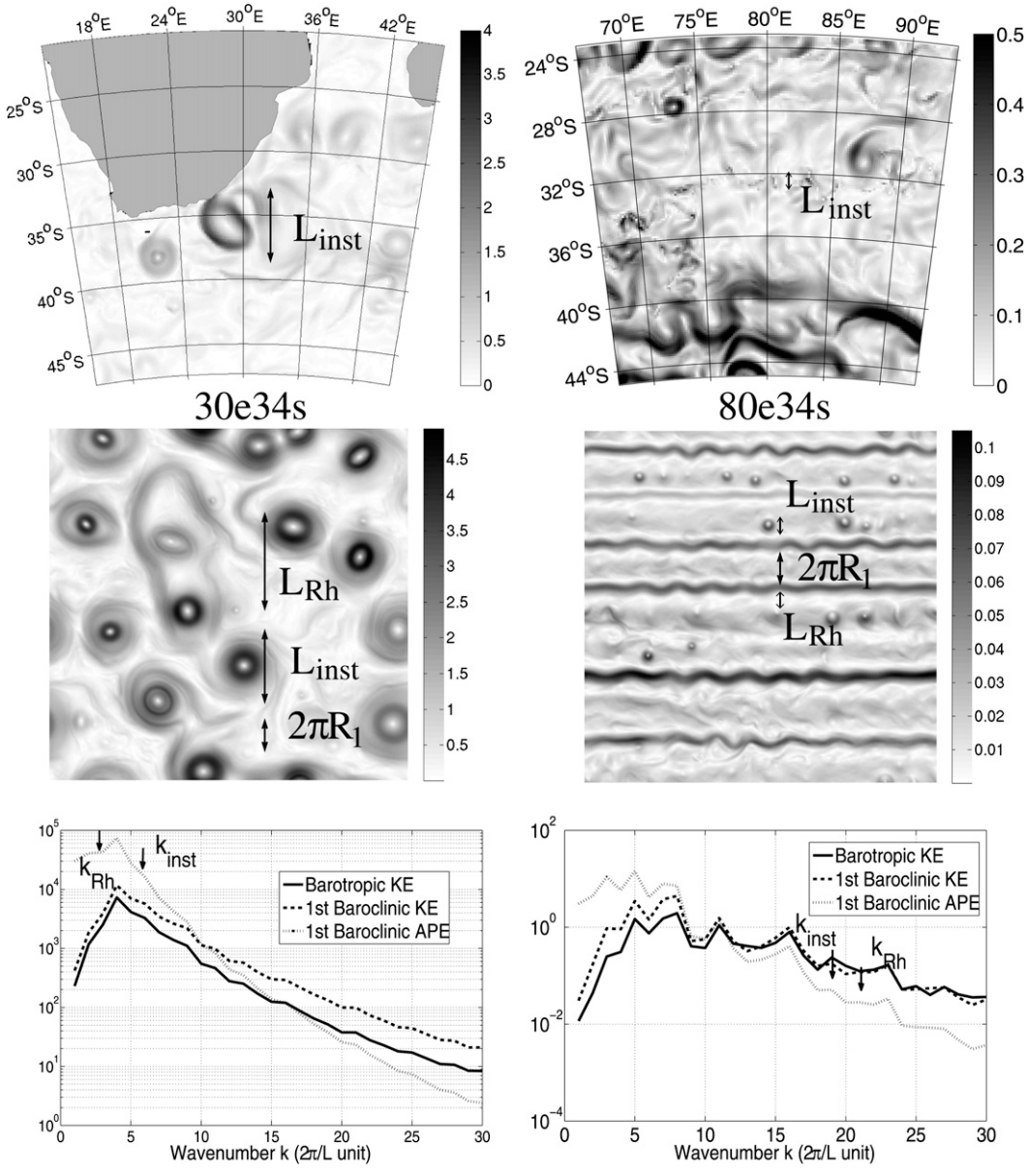

FIG. 10. Snapshots of surface speed (m s^{-1}) in (top) MESO and (bottom) the corresponding QG simulations. At a given location, the domain length is the same for the MESO and QG snapshots: namely, $L = 64R_1$. (bottom) Energy spectra from the MESO simulation. Also shown are the relevant length scales (and corresponding wavenumbers), including the linear instability wavelength L_{inst} (the prime denotes a secondary peak in the growth rate), the Rhines scale $2\pi(V/\beta)^{1/2}$, and the first baroclinic wavelength $2\pi R_1$ (wavenumber $k_1 \approx 10$ on the spectrum). The QG runs presented are the one with high bottom friction ($r = 100r_{\text{control}}$) for point 34°S, 30°E and the one with thermal damping for point 34°S, 80°E; see Table 2 for more details.

Spectra of barotropic and first baroclinic KE and the APE are plotted in Figs. 10 and 11 (bottom). These spectra support the idea that there is a moderate inverse cascade for both barotropic and first baroclinic modes: the energy peak is generally larger than the instability wavelength, but only by a factor of a few. The equivalent barotropic nature of the flow is noticeable in these cases: the first baroclinic and barotropic kinetic energy spectra have roughly the same shape. It is also apparent that the total energy is dominated by the available potential energy, which is always at scales larger than the instability wavelength, consistent with a moderate inverse cascade for the available potential energy in the quasi-geostrophic simulations.

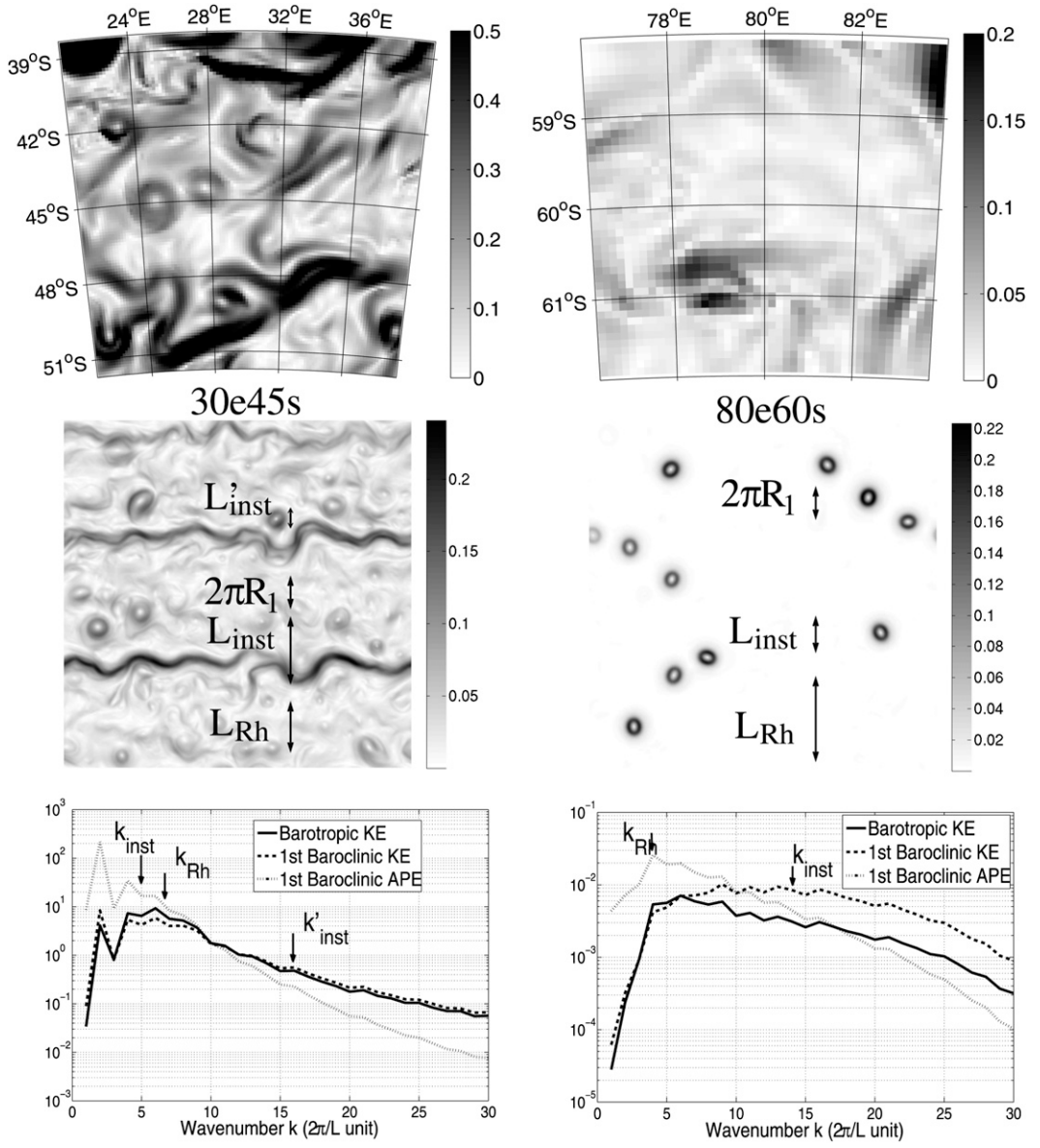

FIG. 11. The QG runs presented with thermal damping. See Fig. 10 for legend and Table 2 for more details.

In regions where β is sufficiently large and where energy levels are sufficiently low, strong eastward jets form and separate regions of homogenized potential vorticity in the upper layers, as in Fig. 10 (right). This is of course consistent with the familiar notion that the beta effect leads to anisotropic flows (Rhines 1975; Vallis and Maltrud 1993). However, the Rhines scale itself ($L_{\mathrm{Rh}} \equiv 2\pi\sqrt{v_{\mathrm{rms}}/\beta}$) does not manifest itself unambiguously in the simulations: one might expect to see a footprint of this length scale in the horizontal dynamics if the flow were fully barotropic, but, perhaps because there is no clear separation between the instability scale and the scale of the eddies, this is not always the case. Point 60°S, 80°E is an exception, as illustrated in Fig. 11: here, the peak in the kinetic energy spectrum occurs at the Rhines scale and corresponds to the zonal jet width in physical space (these zonal jets have a negligible contribution to the instantaneous surface velocity but do appear on a snapshot of the barotropic velocity). This peak is not related to the injection mechanism, because the instability wavelength is at much shorter scale (and corresponds to the size of the surface-intensified coherent rings in physical space). In that case, there is effectively a clear inverse cascade for the barotropic mode, with a cascade arrest at about the Rhines scale.

d. On the locality hypothesis

The QG simulations performed at different locations display very different flow structures. Although the presence of the beta effect and surface-intensified stratification are clearly key ingredients in setting some of the flow properties, as is bottom friction, these parameters vary only very slowly in space (stratification varies mostly in the meridional direction) and are unlikely to be responsible for the different regimes. By contrast, mean shear profiles vary quite rapidly and are characterized by quite fine-grained structures (Fig. 5); changing the mean shear (e.g., by setting the mean zonal or meridional velocities to zero) strongly affects the turbulent properties.

We conclude that in our QG simulations, the transition from one regime of self-organization (e.g., dominated by zonal jets) to another regime (e.g., dominated by coherent rings) occurs over the horizontal scales of variations of the mean vertical shear. This shows the limitation of locality hypothesis: in regions characterized by strong spatial variations of the mean shear (i.e., close to western boundary currents or to regions where topographic steering is important), eddy properties at one point may be due to instabilities occurring in the same area but at a different place. This picture is consistent with the fact that EKE maps are smooth (see, e.g., Fig. 1, bottom).

5. Summary and conclusions

The aims of this paper have been to make progress in understanding the processes that set the length scale, vertical structure, and magnitudes of oceanic eddies. We have proceeded by supposing the mean flow is given, either from observations or, as in this paper, from a primitive equation model. Using the profiles of shear and stratification at various locations, we compute the linear instability properties of the flow at all locations and integrate a fully nonlinear quasigeostrophic model driven by the mean state at six particular locations. The degree to which the latter produces an eddy field of similar energy, scale, and structure to that at the driving location in the MESO simulation can be taken as a test of the ''locality hypothesis'' (i.e., the idea that eddy statistics are a function of the local mean state). Consistent with this hypothesis, neither the linear stability analysis nor nonlinear integrations take into account the horizontal shear or time dependence of the flow, nor do they allow eddies to advect in or out of the region.

Although only a only few ingredients have been taken into account, a number of the nonlinear quasigeostrophic simulations compare well with the primitive equation simulations in the structure, scale, and magnitude of the eddies. We conjecture that, in regions characterized by strong and fast instabilities (time scales from days to weeks), the length scale and the regime of self-organization can be interpreted with local, nonlinear quasigeostrophic simulations. However, because the simulations are local, the propagation of eddies away from the source is neglected, and, because the mean flow is imposed, possibly important interactions between eddies and mean flows are neglected. In regions characterized by weak, slow instabilities, the dynamics seem to be governed by eddies coming from more unstable regions. In some regions, artificially high bottom drag or thermal damping were necessary to equilibrate quasigeostrophic simulations, suggesting that the primitive equations are equilibrating by nonlocal mechanisms (e.g., the advection of the eddy field away from a region of instability) or possibly through ageostrophic sources of dissipation.

Perhaps most striking overall is the degree of inhomogeneity of the eddy field in both the quasigeostrophic and primitive equation simulations. In some regions, the flow is clearly very strongly eddying; in some regions, it is less so. In some regions, the flow is dominated by coherent structures (jets and rings); in some regions, it is less so. The presence of such coherent structures in at least three of the six cases investigated is surprisingly well reproduced by the quasigeostrophic simulations. The flow dynamics is generally more reminiscent of the phenomenology of equivalent barotropic, reduced gravity quasigeostrophic turbulence than of barotropic turbulence on a β plane: in modal representation, barotropic and baroclinic flows are both dominant, but, in regimes of high bottom friction, their ratio is such that the flow has the structure of a two-vertical-layer system with most of the dynamics confined in the upper layer.

Regarding the horizontal scale of the eddies, we find that typically the eddy scale is somewhat larger than the instability scale, suggesting a moderate inverse cascade rather than an extended one (although the production of zonal jets may be regarded as an extended transfer of energy to grave horizontal scales in the zonal direction). The final scale of the eddies is determined by a combination of bottom drag, the formation of coherent structures, and Rossby wave scattering, with no single effect dominating anywhere. Regarding the vertical structure of the eddies, nearly all of the kinetic energy is in the barotropic and first baroclinic modes. In some regions, there is a residual of surface-intensified flow, which seems to arise from the linear instability problem, for which the fastest-growing mode is commonly surface intensified. Evidently, the vertical structure of the eddies are in something of an intermediate regime between the profile set by the most unstable mode and a tendency for barotropization and first baroclinization. The nonlinear

integrations generally show more agreement with the primitive equations, in terms of horizontal and vertical scales and structure, than do purely linear instability calculations. Nonetheless, in many cases the fully equilibrated flows do show a residual signature of the linear instability, particularly in the near-surface enhancement of the eddy flow.

The inhomogeneity of the flow and the lack of a single flow regime—whether linear or highly turbulent—suggests that we should not seek a single, all-encompassing theory of mesoscale eddies. Nor would it be correct to base a parameterization of mesoscale eddy fluxes purely on the basis of linear theory or purely on the presumption that the flow is in a fully developed state of geostrophic turbulence. The bulk of the Southern Ocean seems somewhere between these extremes. Ingredients for a full understanding of the eddy field must come from linear theory, geostrophic turbulent cascade phenomenology, and theories explaining the emergence and the dynamics of coherent structures. A greater degree of idealization than the setting of this paper, but with more realism than previous studies with idealized profiles of shear and stratification, may be needed to make progress in this area, and we are currently pursuing this, with the hope of bridging the gap between idealized studies of geostrophic turbulence and the real ocean.

Acknowledgments. We thank Ross Tulloch for interesting discussions and two anonymous reviewers that helped to improve the presentation of the manuscript. This work was supported by DOE Grant DE-SC0005189 and NOAA Grant NA08OAR4320752.

APPENDIX

Linear Instability Computations

We linearize the quasigeostrophic Eq. (4a) and look for normal modes of the form

$$\psi = \mathrm{Re}[\tilde{\psi}_{k,l}(z)e^{-i\omega_{k,l}t+ikx+ily}]. \quad (6)$$

The growth rate $\mathrm{I}\omega_{k,l}$ (where I denotes the imaginary part) and corresponding modes $\tilde{\psi}_{k,l}(z)$ are computed for a range of wavenumbers k and l such that $1/(5R_1) > (k^2 + l^2)^{1/2} < 5/R_1$, following Tulloch et al. (2011). The maximum growth rate is defined as

$$\omega_{\mathrm{inst}} = \max_{l,k}[\mathrm{I}(\omega_{k,l})],$$

and the corresponding instability wavelength is $L_{\mathrm{inst}} = 2\pi(k_{\mathrm{inst}} + l_{\mathrm{inst}})^{-1/2}$.

REFERENCES

Arbic, B. K., and G. R. Flierl, 2004a: Baroclinically unstable geostrophic turbulence in the limits of strong and weak bottom Ekman friction: Application to midocean eddies. *J. Phys. Oceanogr.,* **34,** 2257–2273.

——, and ——, 2004b: Effects of mean flow direction on energy, isotropy, and coherence of baroclinically unstable beta-plane geostrophic turbulence. *J. Phys. Oceanogr.,* **34,** 77–93.

Berloff, P., I. Kamenkovich, and J. Pedlosky, 2009a: A mechanism of formation of multiple zonal jets in the oceans. *J. Fluid Mech.,* **628,** 395–425.

——, ——, and ——, 2009b: A model of multiple zonal jets in the oceans: Dynamical and kinematical analysis. *J. Phys. Oceanogr.,* **39,** 2711–2734.

Bretherton, F., 1966: Critical layer instability in baroclinic flows. *Quart. J. Roy. Meteor. Soc.,* **92,** 325–334.

Capet, X., P. Klein, B. L. Hua, G. Lapeyre, and J. C. McWilliams, 2008: Surface kinetic energy transfer in SQG flows. *J. Fluid Mech.,* **604,** 165–174.

Chelton, D. B., M. G. Schlax, R. M. Samelson, and R. A. de Szoeke, 2007: Global observations of large oceanic eddies. *Geophys. Res. Lett.,* **34,** L15606, doi:10.1029/2007GL030812.

Dewar, W., 1998: Topography and barotropic transport control by bottom friction. *J. Mar. Res.,* **56,** 295–328.

Farrell, B., and P. Ioannou, 1999: Perturbation growth and structure in time-dependent flows. *J. Atmos. Sci.,* **56,** 3622–3639.

Ferrari, R., S. M. Griffies, G. Nurser, and G. K. Vallis, 2010: A boundary value problem for the parameterized mesoscale eddy transport. *Ocean Modell.,* **32,** 143–156.

Flierl, G. R., and J. Pedlosky, 2007: The nonlinear dynamics of time-dependent subcritical baroclinic currents. *J. Phys. Oceanogr.,* **37,** 1001–1021.

Fu, L. L., and Y. Menard, 1983: Recent progress in the application of satellite altimetry to observing the mesoscale variability and general circulation of the oceans. *Rev. Geophys. Space Phys.,* **21,** 1657–1666.

Gent, P. R., J. Willebrand, T. J. McDougall, and J. C. McWilliams, 1995: Parameterizing eddy-induced transports in ocean circulation models. *J. Phys. Oceanogr.,* **25,** 463–474.

Gill, A. E., J. S. A. Green, and A. Simmons, 1974: Energy partition in the large-scale ocean circulation and the production of midocean eddies. *Deep-Sea Res.,* **21,** 499–528.

Grianik, N., I. M. Held, K. S. Smith, and G. K. Vallis, 2004: The effects of quadratic drag on the inverse cascade of two-dimensional turbulence. *Phys. Fluids,* **16,** 1–16.

Haidvogel, D. B., and I. M. Held, 1980: Homogeneous quasi-geostrophic turbulence driven by a uniform temperature gradient. *J. Atmos. Sci.,* **37,** 2644–2660.

Hallberg, R., and A. Gnanadesikan, 2006: The role of eddies in determining the structure and response of the wind-driven Southern Hemisphere overturning: Results from the Modeling Eddies in the Southern Ocean (MESO) project. *J. Phys. Oceanogr.,* **36,** 2232–2252.

Haynes, P., D. Poet, and E. Shuckburgh, 2007: Transport and mixing in kinematic and dynamically consistent flows. *J. Atmos. Sci.,* **64,** 3640–3651.

Held, I. M., and V. D. Larichev, 1996: A scaling theory for horizontally homogeneous, baroclinically unstable flow on a beta plane. *J. Atmos. Sci.,* **53,** 946–952.

Isern-Fontanet, J., E. García-Ladona, and J. Font, 2003: Identification of marine eddies from altimetric maps. *J. Atmos. Oceanic Technol.,* **20,** 772–778.

——, ——, and ——, 2006: Vortices of the Mediterranean Sea: An altimetric perspective. *J. Phys. Oceanogr.,* **36,** 87–103.

Jiménez, J., and A. Guegan, 2007: Spontaneous generation of vortex crystals from forced two-dimensional homogeneous turbulence. *Phys. Fluids,* **19,** 085103, doi:10.1063/1.2757713.

Lapeyre, G., 2009: What vertical mode does the altimeter reflect? On the decomposition in baroclinic modes and on a surface-trapped mode. *J. Phys. Oceanogr.,* **39,** 2857–2874.

——, and I. M. Held, 2003: Diffusivity, kinetic energy dissipation, and closure theories for the poleward eddy heat flux. *J. Atmos. Sci.,* **60,** 2907–2916.

——, and P. Klein, 2006: Dynamics of the upper oceanic layers in terms of surface quasigeostrophy theory. *J. Phys. Oceanogr.,* **36,** 165–176.

Maltrud, M., and G. K. Vallis, 1991: Energy spectra and coherent structures in forced two-dimensional and geostrophic turbulence. *J. Fluid Mech.,* **228,** 321–342.

Marshall, D., 1995: Topographic steering of the Antarctic Circumpolar Current. *J. Phys. Oceanogr.,* **25,** 1636–1650.

Maximenko, N. A., B. Bang, and H. Sasaki, 2005: Observational evidence of alternating zonal jets in the world ocean. *Geophys. Res. Lett.,* **32,** L12607, doi:10.1029/2005GL022728.

Merryfield, W. J., 1998: Effects of stratification on quasi-geostrophic inviscid equilibria. *J. Fluid Mech.,* **354,** 345–356.

Pedlosky, J., 1984: The equations for geostrophic motion in the ocean. *J. Phys. Oceanogr.,* **14,** 448–456.

Rhines, P. B., 1975: Waves and turbulence on a β-plane. *J. Fluid Mech.,* **69,** 417–443.

——, 1979: Geostrophic turbulence. *Annu. Rev. Fluid Mech.,* **11,** 401–441.

Richards, K. J., N. A. Maximenko, F. O. Bryan, and H. Sasaki, 2006: Zonal jets in the Pacific Ocean. *Geophys. Res. Lett.,* **33,** L03605, doi:10.1029/2005GL024645.

Salmon, R., 1980: Baroclinic instability and geostrophic turbulence. *Geophys. Astrophys. Fluid Dyn.,* **15,** 167–211.

Scott, R. B., and F. Wang, 2005: Direct evidence of an oceanic inverse kinetic energy cascade from satellite altimetry. *J. Phys. Oceanogr.,* **35,** 1650–1666.

Sinha, B., and K. J. Richards, 1999: Jet structure and scaling in Southern Ocean models. *J. Phys. Oceanogr.,* **29,** 1143–1155.

Smith, K. S., 2005: Tracer transport along and across coherent jets in two-dimensional turbulent flow. *J. Fluid Mech.,* **544,** 133–142.

——, 2007a: Eddy amplitudes in baroclinic turbulence driven by nonzonal mean flow: Shear dispersion of potential vorticity. *J. Phys. Oceanogr.,* **37,** 1037–1050.

——, 2007b: The geography of linear baroclinic instability in Earth's oceans. *J. Mar. Res.,* **65,** 655–683.

——, and G. K. Vallis, 2001: The scales and equilibration of midocean eddies: Freely evolving flow. *J. Phys. Oceanogr.,* **31,** 554–571.

——, and ——, 2002: The scales and equilibration of midocean eddies: Forced dissipative flow. *J. Phys. Oceanogr.,* **32,** 1699–1721.

Spall, M. A., 2000: Generation of strong mesoscale eddies by weak ocean gyres. *J. Mar. Res.,* **58,** 97–116.

Stammer, D., 1997: Global characteristics of ocean variability estimated from regional TOPEX/POSEIDON altimeter measurements. *J. Phys. Oceanogr.,* **27,** 1743–1769.

Thompson, A. F., 2010: Jet formation and evolution in baroclinic turbulence with simple topography. *J. Phys. Oceanogr.,* **40,** 257–278.

——, and W. R. Young, 2006: Scaling baroclinic eddy fluxes: Vortices and energy balance. *J. Phys. Oceanogr.,* **36,** 720–738.

——, and ——, 2007: Two-layer baroclinic eddy heat fluxes: Zonal flows and energy balance. *J. Atmos. Sci.,* **64,** 3214–3231.

Treguier, A. M., and B. L. Hua, 1988: Influence of bottom topography on stratified quasi-geostrophic turbulence in the ocean. *Geophys. Astrophys. Fluid Dyn.,* **43,** 265–305.

——, and J. C. McWilliams, 1990: Topographic influences on wind-driven, stratified flow in a β-plane channel: An idealized model for the Antarctic Circumpolar Current. *J. Phys. Oceanogr.,* **20,** 321–343.

Tulloch, R., J. Marshall, C. Hill, and K. S. Smith, 2011: Scales, growth rates, and spectral fluxes of baroclinic instability in the ocean. *J. Phys. Oceanogr.,* **41,** 1057–1076.

Vallis, G. K., 2006: *Atmospheric and Oceanic Fluid Dynamics*. Cambridge University Press, 745 pp.

——, and M. E. Maltrud, 1993: Generation of mean flows and jets on a beta plane and over topography. *J. Phys. Oceanogr.,* **23,** 1346–1362.

Venaille, A., and F. Bouchet, 2011: Oceanic rings and jets as statistical equilibrium states. *J. Phys. Oceanogr.,* in press.

Visbeck, M., J. Marshall, T. Haine, and M. Spall, 1997: Specification of eddy transfer coefficients in coarse-resolution ocean circulation models. *J. Phys. Oceanogr.,* **27,** 381–402.

Wunsch, C., 1997: The vertical partition of oceanic horizontal kinetic energy. *J. Phys. Oceanogr.,* **27,** 1770–1794.